LAWRENCE
LIVERMORE
NATIONAL
LABORATORY

LLNL-JRNL-560311

Phase Transition in BCx system under High-Pressure and High-Temperature: Synthesis of Cubic Dense BC3 Nanostructured Phase

P. V. Zinin, L. C. Ming, H. A. Ishii, R. Jia, T. Acosta, E. Hellebrand

June 7, 2012

Journal of Applied Physics

Phase Transition in BCx system under High-Pressure and High-Temperature: Synthesis of Cubic Dense BC_3 Nanostructured Phase

P. V. Zinin[1], L. C. Ming[1], H. A. Ishii[2], R. Jia[1], T. Acosta[1], E. Hellebrand[3],

[1]Hawaii Institute of Geophysics and Planetology, University of Hawaii, Honolulu, Hawaii, USA

[2]Institute of Geophysics and Planetary Physics, Lawrence Livermore National Laboratory, Livermore, California, USA

[3]Department of Geology and Geophysics, University of Hawaii, Honolulu, Hawaii, USA

E-mail: zinin@soest.hawaii.edu

Abstract. We synthesized a cubic BC_3 (c-BC_3) phase, by direct transformation from graphitic phases at a pressure of 39 GPa and temperature of 2200 K in a laser-heated diamond anvil cell (DAC). A combination of x-ray diffraction (XRD), electron diffraction (ED), transmission electron microscopy (TEM) imaging, and electron energy loss spectroscopy (EELS) measurements lead us to conclude that the obtained phase is hetero-nano-diamond, c-BC_3. High-resolution TEM (HRTEM) imaging of the c-BC_3 specimen recovered at ambient conditions demonstrates that the c-BC_3 is a single, uniform, nanocrystalline phase with a grain size of about 3-5 nm. The EELS measurements show that the atoms inside the cubic structure are bonded by sp^3 bonds. The zero-pressure lattice parameter of the c-BC_3 calculated from diffraction peaks was found to be a = 3.589 ± 0.007 Å. The composition of the c-BC_3 is determined from EELS measurements. The ratio of carbon to boron, C/B, is approximately 3 (2.8 ± 0.7).

I. Introduction

Phase transition under high pressure and high temperature (HPHT) in a BC_x system has recently attracted the interest of researchers for several reasons. First, it is predicted that the incorporation of B atoms into a diamond structure in the B-C system (BC, BC_3, and BC_7) should not lead to a drastic distortion of the cubic cell of a diamond[1, 2]. Recently, several new structures of dense BCx phases were proposed: (a) a diamond-like *t*-BC_2 (*dlt*-BC_2) with a tetragonal lattice originating from the cubic structure[3]; (b) a *c*-BC_3[4-6] with a slightly deformed cubic cell; (c) a tetragonal BC_3 (*t*-BC_3) phase originating from the cubic structure[7]; and (d) three diamond-like BC_3 (*dl*-BC_3) structures (orthorhombic Pmma-a consisting of a sandwich-like "B layer" between C layers, orthorhombic Pmma-b with B–B bondings, and tetragonal P-4m2[8]); (e) a stable *dl*-BC_5 compound with a slightly distorted cubic cell[9, 10] and *dl*-BC_5 with possible two Pmma structures[11]; and (f) *dl*-BC_7[12-14]. These dense BCx phases were predicted to be superhard[1-3] and, more importantly, they should exhibit interesting electrical properties. Unlike diamond, which is an isolator, the dense BC_x phases may be conductors or superconductors: the *dlt*-BC_2 phase was predicted to be a conductor with three-dimensional conductivity[3]; the *t*-BC_3 phase should exhibit a sandwich-like metal and/or insulator layered structure with the anisotropic conductivity on the basal planes formed by the metallic CBC blocks[7], *c*-BC_3, or *dl*-BC_3 structures that would behave as a metal at ambient conditions[6], and was predicted to be a superconductor at low temperatures[4, 5, 8]; the *dl*-BC_5 phases should exhibit metallic[9] or hole conducting[11] behavior at ambient conditions and superconductor behavior at low temperatures[10]; and the *dl*- BC_7 phase was predicted to be a superconductor[13, 14]. A combination of the high elastic moduli and various electrical properties that can be tuned by varying the B/C ratio of the dense BCx phases makes these phases attractive for a broad range of applications and industries, especially the electronics

industry. Therefore, it would be of interest to understand the high pressure and high temperature diagram of phase transitions for the BC_x system.

A prior attempt to convert graphite-like BC_3 (*g*-BC_3) into a cubic phase in the B-C system at moderate pressure and temperature conditions, 20 GPa and 2300 K, in a multianvil press led to the decomposition of the *g*-BC_3 phase into B_4C and boron-doped diamond with 1.8 at. % B[15]. To avoid this decomposition, we studied the phase transformation BC_x phase in a DAC under pressures higher than 40 GPa for the following reasons: (a) XRD data suggested that at 2230±140 K and high pressure of 45 GPa the graphitic phase transformed into cubic $BC_{1.6}$ phase[16]; and (b) measurements of the Raman scattering of the quenched phases demonstrated that graphitic phases transformed into a *dl*-BC_3 phase after laser heating of the *g*-BC_3 phase at 2033 K and 50 GPa[17] (see also Ref.[18]). Recently, researchers claimed to observe a phase transition from graphitic phase to *dl*-BC_5 at 24 GPa and temperature of 2200 K, in a BC_5 system[19]. Despite progress in the understanding of the phase transition in BC_x materials, such as observations of the phase transitions in $BC_{1.6}$, BC_3, and BC_5 under high pressure and high temperature[15-21], we still do not know many important properties of the obtained phases (e.g. atomic, micro-, or nano-structures; elemental composition; and types of chemical bondings). The HPHT conditions of the transition of the graphitic BC_x phase to another phase are also disputable: phase transitions were detected above 35 GPa in Refs. [16-18, 21]; and was not observed in the BC_x system ($1.6 < x \leq 3$) at pressures of 20 GPa[15], 19 GPa[17], and 24 GPa (Ref.[16] and this study). Contrary to abovementioned results, the authors of Ref.[19] claim that at pressures above 20 GPa in the 2000–2500 K range, *g*-BCx phases ($1 < x < 4$) decompose into boron-doped diamond (1–2% of boron) and boron carbides (B_4C and $B_{50}C_2$) that are accompanied by the formation of cubic B-C phases (c-BCz).

The identification of the obtained BC_x phases cannot be made exclusively using x-ray diffraction or Raman spectroscopy. First, if the synthesized HPHT phases contain amorphous micro or nano-grains, these nano-grains would not contribute to the appearance of the XRD pattern of such a phase. In the case of nanostructured phases, the x-ray spectra or Raman spectra are an average of signals scattered from a volume containing numerous nano-grains, some of which could be amorphous. For instance, if the starting BCx phase is decomposed under HPHT conditions on a nano-grain structure consisting of cubic carbon and amorphous boron nano-grains then the x-ray of the obtained phase would be similar to that of diamond. Zhao et al.[22] conducted ED and EELS measurements from a single nano-grain to determine the structure of the BC_2N phase synthesized under HPHT conditions, and they found that *c*-BC_2N nano-grains were surrounded by an amorphous matrix in the quenched specimen. Therefore the stoichiometry, nanostructure, chemical purity, and homogeneity of BC_x phases obtained under HPHT conditions can only be unambiguously established by using TEM in conjunction with ED and EELS techniques[22, 23].

We conducted this study to answer the following questions: (a) what HPFT conditions are required to convert a *g*-BC_x phase into a dense BC_x phase; (b) what is the structure of the dense BC_x phases obtained under HPHT conditions; and (c) is there a concentration limit for B atoms below which the *g*-BC_x cannot be transformed into single dense BCx phase under HPHT conditions. Here, we present direct experimental data on the phase transition of the BC_3 system and demonstrate that the phase obtained at 39 GPa and 2200 K in a DAC is a nano-grain phase with a cubic atomic structure (*c*-BC_3) phase bonded with sp^3 bonds. We do this by using by XRD, TEM, ED, EELS, and Raman scattering techniques.

II. Experimental methods

The precursor, graphitic (*g*-BC_3) was prepared by a high-pressure thermal chemical vapor deposition (HPCVD) method using C_2H_2, BCl_3 (as carbon and boron sources) and H_2 (30 mbar, 1225° C)[24]. A symmetrical DAC equipped with a pair of type I brilliant-cut diamond anvils (with 350 μm culets) was used in the experiment. A fully hardened stainless steel gasket of 250 μm thick was first indented to 40 μm, and then a hole with a diameter of 130 μm was drilled, which served as the sample chamber. Sodium chloride (NaCl) was loaded between the specimen and the diamond anvil for thermal isolation to ensure efficient laser heating of the specimen. Pressure was measured using positions of the XRD peaks of NaCl. The pressure- and temperature-induced phase transformation of *g*-BC_3 was studied using double-sided laser-heated DACs and angle-dispersive powder XRD. The duration of the laser heating was around 30 s. The XRD measurements were performed using a monochromatic synchrotron radiation source at the 16-ID-B beamline of the HPCAT facility and at the GeoSoilEnviro-CARS, station 13ID-B at the Advanced Photon Source (APS), Argonne National Laboratory (ANL), where diode pumped fiber lasers with an adjustable total power up to 200W at 1.064μm wavelength are available for double-sided laser-heating in the DAC [25]. With such heating, the sample temperature gradients can be minimized both radially and axially within the DAC and, as a result, a thick sample can be heated uniformly, thus leading to a higher yield of the dense phase[26].

Three specimens were synthesized form the same piece *g*-BC_3: (a) specimen *A* was synthesized at a temperature of 2020 K and pressure of 24 GPa; (b) specimen *B* was synthesized at a temperature of 1980 K and pressure of 44 GPa; and (c) specimen *C* was synthesized at a temperature of 2200 K and pressure of 39 GPa. Elemental composition was measured by the EELS technique only for specimen *C* and it was found to be BC_3 (see section on TEM/EELS

measurements). Because all three specimens were synthesized from the same piece of the *g*-BC_3 phase, and assuming that composition has not changed during the laser heating, we postulate that the composition of all three specimens is BC_3. For XRD measurements, the recovered BC_3 specimens *A* and *B* in the gasket were gently rinsed in water to remove the thermally insulating NaCl layers above and below the specimens. For TEM analysis, the following procedure was developed. After quenching, an x-ray pattern of the recovered specimen *C* in the gasket was measured prior to NaCl removal. After x-ray measurements, one of the sample sides (covered by NaCl) was first fixed with an epoxy resin. Then, the gasket was turned over and gently rinsed in water to remove the thermally insulating NaCl layers located above and below the BC_3 specimen. Then, the specimen was covered with epoxy resin and polished (using 0.3 micron diamond paste) until an optically flat surface on the sample was exposed.

In order to prepare an electron-transparent thin section of the small (less than 100 μm) and superhard[40] recovered BC_x specimen, a Focused Ion Beam (FIB) preparation of a TEM section was carried out using an FEI Nova NanoLab600 dual beam FIB at the Lawrence Livermore National Laboratory (LLNL). The LLNL FIB has an upgraded Sidewinder column, *in situ* micromanipulator, and *in situ* Pt deposition to protect the region being extracted from direct ion beam damage. A few-microns thick slab was extracted by ion milling and attached by micromanipulator to a TEM half-grid where it was thinned to electron transparency (<100 nm). The estimated final thickness is 50 nm based on edge-on secondary electron imaging.

The FIB-prepared TEM thin section was examined with an FEI Titan^3 G2 60-300 dual-C_s-aberration-corrected, monochromated (scanning) transmission electron microscope (STEM) at the LLNL. Imaging, ED, and EELS were carried out at 300 kV accelerating voltage with a high resolution Tridiem Gatan imaging filter (GIF) capable of sub-100 meV energy resolution and 0.8

Å electron probe spatial resolution. A FIB section prepared from a B_4C standard was used to establish the EELS fitting regions used to quantify the recovered BC_3 sample under identical experimental conditions. The EELS quantification of edge jump ratios (integrated over a post-edge energy window) was carried out using a power-law background fit and calculated Hartree-Slater cross-sections with Gatan Digital Micrograph software (Gatan, Inc., Pleasanton, CA). The B_4C standard composition determined in this manner was B = 79.70 ± 10.3 at%, C = 20.30 ± 2.7 at%. The ratio of sample thickness to plasmon mean free path for the regions from which the core-loss edge EELS were acquired was typically $t/\lambda = 0.5$. Spectra were acquired at 0.1 eV/channel dispersion over both B and C core loss edges for elemental quantification with EELS energy resolution of 0.9 eV, as measured experimentally with the full width at half maximum of the zero loss peak through the sample. Higher resolution spectra were also acquired at 0.02 eV/channel dispersion over near edge regions to check for π^* and σ^* bonding with EELS energy resolution of 0.2 eV, as measured by the full width at half maximum of the zero loss peak. Energy calibration was carried out relative to the zero loss peak before and after each EELS spectrum acquisition. Electron diffraction was collected from the same regions. For electron diffraction, internal calibration of *d*-spacings was provided by the FIB-deposited Pt layer with $d_{(111)}$=2.27 Å.

The Raman scattering measurements were performed using a confocal Raman microscope confocal Raman system (WiTec alpha300). With the confocal microscope, the Raman spectra were excited by an Nd:YAG green (532-nm) laser (Coherent Compass, Dieburg, Germany). Peak-fitting analysis (dashed lines in the figures) was performed using Grams Software (version 8.0, Thermo Fisher Scientific, Inc.), and a background subtraction procedure was applied for the Raman spectra.

III. Results

III. A. Characterization of the starting graphitic BC_3 phase

Figure 1a shows an XRD pattern of the starting *g*-BC_3 phase at ambient conditions. A weak peak at 2.385 Å is believed to be from rare B_4C remains, which were left in the process of synthesis[27]. The *g*-BC_3 phase is not a perfect graphitic crystal. Instead, it is a random layer of solids (turbostratic graphite[28, 29]) for which the theory of the x-ray diffraction was developed by Franklin[28, 29] and Warren[30]. In turbostratic graphite, the graphite-like layers are stacked in parallel groups but are not otherwise mutually orientated. If x_1 and x_2 are the axes in the graphite layer, and x_3 is normal to the graphitic then an x-ray pattern of the turbostratic graphite should have a crystalline reflection of type (*00l*), two-dimensional lattice reflection of type (*hk*0), and no general reflections (*hkl*) ($l \neq 0$) because the three-dimensional structure of crystalline graphite is absent[29]. The two-dimensional lattice reflections are referred to by only two Miller indices (*hk*). The appearance of the XRD pattern of the *g*-BC_3 phase is similar to that of B-C[31] and B-C-N turbostratic graphitic phases[32]; there is a broad peak at 3.450 Å corresponding to the (*001*) peak for turbostratic BC_3[33]. The (*002*) peak is not detectable in the XRD pattern. The positions of the three other peaks centered at 2.128, 1.229, and 1.065 Å on the x-ray pattern can be indexed as two-dimensional lattice reflections of type (*10*), (*11*), and (*20*). The XRD pattern of *g*-BC_3 does not match a cubic structure but it is well indexed using a hexagonal cell with the lattice parameters $a = 2.459 \pm 0.006$ Å and $c = 3.45 \pm 0.37$ Å. The value of the lattice parameter *a* is in a good agreement with that measured experimentally, 2.474 Å [34], and is less than that predicted theoretically, 2.563 Å [35]. If the *c*-axis is doubled, the *c* parameter of the unit cell of *g*-BC_3 is close to that of graphite (6.714 Å) (JCPDS # 23-64). The relative intensities of the XRD peaks in

the *g*-BC_3 phase are different from those of graphite. Typically, the (*001*) peak of turbostratic graphitic phases is the most intense[32, 33]. This indicates that the *g*-BC_3 starting material used in this study probably has very different stacking layers of B-C hexagons along the *c*-axis.

The Raman scattering pattern and optical image of the *g*-BC_3 phase are presented in Fig. 1b. The specimen is black and non-transparent (see insert in Fig. 1b). The spectrum has two peaks, broad bands at 1346 and 1581 cm^{-1}, that are characteristic of disordered graphite amorphous carbon[36, 37]. Recently, hexagonal sheets of BC, BC_3, and BC_7 were examined theoretically and their vibration energies compared to those of BCx graphenes[35]. Calculations on various *g*-BC_x structures indicate that the origin of the peaks centered at 1580–1590 cm^{-1} for *g*-BC_x phases is similar to that of the E_{2g} Raman active mode of graphite[36], also called a *G* peak. Theoretical simulations also demonstrate that the next highest energy band of *g*-BC_x phases, around 1350 cm^{-1}, is a Raman active mode and associated with *E* vibrations[35]. A strong peak around 1350 cm^{-1}, which represents the *D* mode, is usually detected in disordered graphite[37]. In graphite, the *D* peak is due to the breathing modes of sp^2 atoms in rings and its intensity is associated with the size of the sp^2 carbon clusters[37]. According to theoretical simulations, the *D* band in *g*-BC_x phases is associated with Raman active vibrations of the B-C ring[35]. Positions of the *G* and *D* modes of *g*-BC_3 phase excited with a green laser (Fig. 1b) are close to theoretical values for *D* and *G* bands[35], which are 1348 and 1555 cm^{-1}, respectively.

III. B. Synthesis of the cubic BC_3 phase

As a result of theoretical consideration of the stability of cubic BC_x phases, Moussa and Cohen suggested keeping the temperature to a minimum for a successful synthesis of cubic BC_x (*c*-BC_x) phases[5, 36]. Because the *c*-BC_x phases are not thermodynamically stable (meta-stable), at

high temperatures boron atoms can find lower energy positions by breaking their sp^2/sp^3 bonds and diffusing[5, 38]. Because the primary diffusion channel for boron in *g*-BC_x phases is interstitial in nature, high pressures might dramatically reduce the possibility of this diffusion process[38]. Therefore, our strategy in the HPHT experiments was to maintain high pressure and keep the temperature to a minimum in order to achieve the formation of the diamond-like phases. An indication of the minimum pressure was provided by the theoretical simulations of Zhou *et al*., who predicted that *g*-BC_3 should transform into *c*-BC_3 at pressures above 35 GPa[39].

Figure 2 shows the XRD pattern and Raman spectrum of specimen *A*, which was synthesized at 24 GPa and a temperature of 2020 K. XRD and Raman scattering measurements of specimen *A* indicate that it has a disordered graphitic structure. The weak peak at 3.735 Å is from the B_4C phase (*012*) in the starting material. The (*021*) peak of B_4C at 2.38 Å is hidden by a shoulder of the 2.129 Å peak of specimen *A*. The (*001*) graphitic peak becomes less intensive and its position moves to 3.241 Å, indicating the shortening of interlayer distances. A possible explanation for the shortening of the interlayer spacing is that the pressure of 24 GPa is not enough to keep some of boron atoms from diffusing between the graphitic layers at temperature of 2020 K. These boron atoms may create interstitial boron structures[40] and shorten interlayer spacing. The positions of the (*10*), (*11*), and (*20*) peaks (Fig. 2a) coincide with those of the starting *g*-BC_3 phase (Fig. 1). The XRD pattern of specimen *A* can be indexed using a hexagonal unit cell with lattice parameters: $a = 2.463 \pm 0.04$ Å; $c = 3.241 \pm 0.045$ Å. The Raman spectrum of specimen *A* is given in Fig. 2b, showing two broad modes at 1350 and 1578 cm^{-1}, which are the *D* and *G* modes, respectively, typical of graphitic materials.

We synthesized a cubic BC_3 (*c*-BC_3) phase, specimen *B*, by a direct transformation from a graphitic phase at a pressure of 44 GPa and a temperature 1980 K in a laser-heated DAC. The

pressure dropped from 44 GPa to 37 GPa after laser heating, indicating that a phase transition had indeed taken place. The XRD patterns of specimen *B* before and after laser heating are shown in Fig. 3. A small peak (Fig. 3) sitting on the shoulder of the (*110*) peak of NaCl (B2) is characteristic of diamond-like phases and its appearance indicates that the graphitic phase was converted to diamond-like phase during laser heating. The peak of the *g*-BC_3 phase at 44 GPa before heating are weak compared to those of the NaCl and difficult to identify in the XRD pattern (Fig. 3).

Specimen *B* was quenched after laser heating and was taken out of the DAC. Then the NaCl was removed from the gasket (see section II) and XRD measurements were conducted. The XRD pattern of specimen *B* in a gasket is shown in Fig. 4a. The (*001*) graphitic peak is absent from the XRD pattern and two weak peaks at 3.734 and 2.347 Å are believed to be from the B_4C phase remaining from the starting material, indicating that B_4C remains intact, untransformed, and uncrystallized at a pressure of up to 44 GPa. The four sharp peaks at 2.075, 1.269, 1.083, and 0.889 Å are indexed as the (*111*), (*220*), (*311*), and (*400*) peaks, respectively, of the cubic unit cell with lattice parameter, $a = 3.589 \pm 0.007$ Å. Together with their respective intensities, the positions of the peaks are in good agreement with those in the diamond structure with both boron and carbon atoms randomly distributed in eight positions in the diamond-like structure. The zero-pressure lattice parameter of the cubic phase obtained in this study is larger than that of diamond (i.e., a =3.5667 Å), which is consistent with the theoretical prediction[1].

The Raman spectrum of the cubic *c*-BC_3 and is shown in Fig. 4b. The Raman spectrum of the *c*-BC_3 phase is also different from that of the starting *g*-BC_3 phase (Fig. 1b), which supports the occurrence of a phase transition. It displays a broad peak at 420 cm^{-1}, a second peak at 1188 cm^{-1}, two broad peaks at 678 and 1040 cm^{-1}, and a much narrower peak around 1280 cm^{-1}. The

Raman spectrum of the *c*-BC_3 is similar to that measured previously[17] where tentative assignment was discussed. Analysis of the Raman spectra of the diamond-like phases, BC_x phases, and those of boron carbide (α-boron) shows that the most intense peaks, 1085 cm^{-1} in $B_{4.3}C$ and 795 cm^{-1} in α-boron, are not seen in the Raman spectra of the *c*-BC_3[17]. The most intense peak at 420 cm^{-1} can be attributed to the Raman active stretching modes of B-B dimers[17, 21]. The second most intense peak at 1188 cm^{-1} may have the same origin as the 1211 cm^{-1} peak of the *c*-$BC_{1.6}$ phase and the 1231 cm^{-1} peak of the *dl*-BC_3 phase[17]. The Raman mode centered around 1200 cm^{-1} was detected in heavily boron-doped polycrystalline diamond films[41]. The band position was found to agree well with the maxima in the phonon density of states of the diamond and could be related to a relaxation of the wave vector selection rules[42]. Theoretical analysis of the Raman scattering in heavily doped diamond $C_{64-n}B_n$ showed that the 500 cm^{-1} and 1230 cm^{-1} bands were both superposed bands that include not only C vibrations but also B-B vibrations and B-C vibrations, respectively[43]. The Raman peak at 1188 cm^{-1} has a particular shape (Fig. 4b) with a tail towards lower wave numbers and is characteristic of heavily boron-doped diamonds. Such a shape is associated with Fano resonances described elsewhere[41, 44, 45]. The appearance of this feature on a Raman spectrum can be interpreted as the emergence of a continuum of electronic states interacting with the zone-center phonon (Fano resonances)[45], and is typical for a heavily boron-doped diamond with a boron concentration close to the metal-to-insulator transition. A broad peak around 1040 cm^{-1} can be seen in the Raman spectra of the phase *B* as well as in *c*-$BC_{1.6}$ [16]. It was observed in both a boron-doped diamond and a nanocrystalline diamond[46] but its origin was not discussed. We mentioned that Raman peaks of the *c*-BC_3 phase are broad (see also Ref.[43]) and cannot be used for unique identification of the

phase, however, Raman scattering measurements are a good indicator of the phase transition under high pressure.

For the TEM study, a *g*-BC_3 phase was loaded into the DAC using a special method. The sample was isolated by NaCl, which is used for thermal isolation during laser heating from both the gasket and the diamond anvils (see insert in Fig. 5a). After quenching, the gasket with the specimen was removed from the DAC and x-ray measurements were conducted. The NaCl was later partially replaced by epoxy, which holds the sample in place and enables polishing the specimen in the gasket for TEM measurements. The phase transition of specimen *C* was obtained at a pressure of 39 GPa and temperature of 2200 K in a laser-heated DAC. The inset image in Fig. 5a is an optical image of the specimen in transmission light showing that the synthesized *c*-BC_3 is not optically transparent. An XRD pattern of this specimen is shown in Fig. 5a. The most intense peaks are from the NaCl that is still present in the specimen when XRD was performed and only one peak, (*111*), from the *c*-BC_3 phase can be detected. The position of the (*111*) peak of the *c*-BC_3 phase is 2.070 Å and is similar to that measured for specimen *B*.

The Raman spectrum of specimen *C* is shown in Fig. 5b. It displays a broad peak at 479 cm^{-1}, a second peak at 1302 cm^{-1}, two broad peaks at 680 and 939 cm^{-1}, and a much narrower peak around 1303 cm^{-1}. It is similar to the Raman spectrum of specimen *B* (Fig. 4b), and different from that of the starting graphitic phase that contains only *D* and *G* peaks (Fig. 1b). The Raman spectrum of specimen *C* also indicates that the graphitic phase has been transformed in a diamond-like phase, *c*-BC_3, after HPHT treatment.

III.C. TEM study

The use of Raman scattering and XRD data allows us to confirm that a phase transition occurred and a cubic phase has been synthesized under high pressure and high temperature. The stoichiometry, nanostructure, chemical purity, and homogeneity of our *c*-BC_3 can only be unambiguously established by using TEM in conjunction with EELS [22, 23]. These allow measurement of the elemental composition and determination of the nanocrystalline structure and nature of the chemical bonds from an area of few nanometers. A good example is the synthesis of the cubic BC_2N (*c*-BC_2N) phase. The cubic BC_2N phase system was obtained under HPHT by Knitle et al.[47] and later confirmed by Solozhenko et al.[48]. In their studies, the cubic structure of the BC_2N phases obtained under HPHT conditions was deduced using synchrotron x-ray diffraction[47, 48] and from the positions of the Raman peaks that were close to diamond[47, 49]. However, confirmation of the cubic atomic chemistry, chemical composition, and nanostructure of the BC_2N phase was obtained later by Zhao et al.[22] from a TEM/EELS study of a single BC_2N nano-grain, and then by Langenhorst and Solozhenko[23], who characterized B-C-N samples synthesized under HPHT conditions using a HRTEM, ED, and EELS.

Figure 6 shows a section of specimen *C* (*c*-BC_3) removed by the Focus Ion Beam (FIB) instrument and thinned to electron transparency (~50 nm) for transmission electron microscopy measurements. A high resolution TEM image of the *c*-BC_3 is shown in Fig. 7 and demonstrates that the *c*-BC_3 is a single, uniform, nanocrystalline phase with a grain size of about 3-5 nm. Figure 8 is the electron diffraction pattern of the nanocrystalline *c*-BC_3 measured from the thin section (Fig. 6) showing the same diamond structure as revealed by the synchrotron XRD (Fig. 4(a) and Fig. 5(a)). The three diffraction rings, are consistent with the *d*-spacings (*111*), (*220*), and (*311*), in the diamond structure with the lattice parameter $a = 3.54 \pm 0.05$ Å. This value is in

agreement, within experimental error, with that obtained by more precise XRD technique, a = 3.589 ± 0.007 Å.

EELS is especially suitable for obtaining local chemical composition and chemical bonding information in light element materials. The EELS spectrum of the c-BC_3 phase collected with 0.1 eV/channel dispersion and 0.9 eV energy resolution is shown in Fig. 9. The B-K and C-K edge EELS spectra of the c-BC_3 phase are similar to those of BC_2N phases[22, 23], and diamond and boron containing diamond-like carbon (DLC) films (a-C:B)[50]. The EELS features remain broad, even at higher spectral resolution, which is likely due to the very fine-grained (3-5 nm) nature of the specimen that results in a relatively high fraction of disordered grain boundary sites. The positions of the onset peaks in the B-K and C-K spectra of the cubic B–C–N phases are at 202.2 and 295.2 eV, respectively. The onset energies of the B-K and C-K edges in the EELS spectra of the c-BC_3 phase are at 188 and 289 eV, respectively. The B-K and C-K edge spectra are dominated by sp^3 bonding (1s $\rightarrow$ σ^* transition peaks) and show only weak, vestigial 1s $\rightarrow$ π^* transition peaks below the primary σ^* features. A decrease in the vestigial π^* bonding has been achieved by ion cleaning of the FIB-generated damaged surface layer on the TEM specimen, which indicates that the remnant σ^* peak may be due entirely to FIB sample preparation. In contrast, the π^* peaks are very strong on the EELS spectra of the starting graphitic BC_3 phase[51] and starting graphitic BC_3 phase synthesized by the interaction of benzene and boron trichloride at 800° C[52]. The EELS spectra of boron, B_4C, carbon and boron rich materials are well documented in the literature[53-56].

The EELS quantification of the elemental composition ratio was carried out on the c-BC_3 phase and yielded consistent compositions of B = 26.6 ± 3.4 at% and C = 73.4 ± 9.3 at%. Therefore, the composition of the phase is approximately BC_3 (B/C = 2.8 ± 0.7).

IV. Discussion

The results of the TEM study demonstrate that the *c*-BC_3 phase is nanocrystalline with a small grain size, typically 3-5 nm. Grain sizes of the *c*-BC_3 phase are slightly smaller than those of the nanostructured cubic BC_2N phase (3-8 nm) synthesized by Zhao et al.[22]. The unit cell of the *c*-BC_3 phase is found to be $a = 3.589 \pm 0.007$ Å. X-ray peaks of *c*-BC_3 phase are relatively broad. The experimentally measured unit cell parameter *a*, is close but less than that predicted by Lowther[1] and Moussa and Cohen[5], $a = 3.685$ Å.

High-resolution TEM imaging of the *c*-BC_3 specimen does not show any obvious amorphous phases (Fig. 2). In combination with the electron diffraction pattern (Fig. 8), it demonstrates that the phase obtained under HPHT phase has a cubic atomic structure similar to that of diamond. The EELS measurements (Fig. 9) show that the atoms inside the cubic structure are bonded by sp^3 bonds, which leads us to conclude that the obtained phase is hetero-diamond *c*-BC_3.

The phase diagram of the BC_x phases is not known. For the BC_3 phase, a direct transformation of the *g*-BC_3 phase to a diamond-like *dl*-BC_3 phase was observed in a DAC at high temperature, around 2000 K, and high pressures, 39 GPa, 44 GPa (current paper), and 50 GPa[17]. The transition, graphitic phase to diamond-like phase, was not observed in the BC_3 system at pressures of 20 GPa[15], 19 GPa[17] and 24 GPa (this study). Therefore, available experimental data allow us to determine the pressure-temperature (P-T) conditions in favor of the phase transition in the BC_x system with a high concentration of B:C/B ≤ 3. Transition to the cubic phase occurs at high temperatures (> 2000 K) and high pressures ($\geq$ 39 GPa). At pressures $\leq$ 25 GPa, the graphitic phase transforms into graphitic phase with smaller interlayer spacing

than that of the starting phase. Heating of the graphitic phases to 2300 K using a multianvil at 20 GPa leads to the decomposition of the *g*-BC_3 into graphite and B_4C[15].

These P-T conditions are in contradiction with those reported in Refs. [19, 57] where two important claims were made: (a) that a *dl*-BC_5 phases was synthesized from a graphitic phase at 24 GPa and 2000 K via direct transition; and (b) that "the turbostratic BC_x phases (*t*-BC_x) with ($1 \leq x \leq 4$) decompose into a boron-doped diamond (1–2 at% of boron) and boron carbides (B_4C and $B_{50}C_2$)" under HPHT. It is of interest to consider the origin of the discrepancy between our experimental results and those of Refs.[19, 57]. Is it really feasible that a small variation in the carbon composition of BC_x phase (from $x = 3$ to $x = 5$) could lead to a substantial pressure reduction of such a transition (from 44 GPa to 24 GPa) as claimed in Ref. [19]? We were not able to find any experimental data supporting the synthesis of *dl*-BC_5 phase at 24 GPa. Indeed, the XRD, ED patterns, and EELS spectra as well as TEM images of the synthesized (quenched) phase *dl*-BC_5 are absent in Ref.[19]. The absence of the EELS data simply means that there is no experimental evidence on (a) whether sp^2 bonds in the starting graphitic BCx phase have been transformed to sp^3 bonds in the synthesized phase and (b) the claim in Ref.[19] that the C/B ratio of product of HPHT is equal to 5 (BC_5).

Recent theoretical simulations uncovered three metallic low-energy structures: (i) orthorhombic *Pmma*-a consisting of a sandwich-like "B layer" between C layers; (ii) orthorhombic *Pmma*-b with B–B bondings; and (iii) tetragonal *P-4m2*[7, 8]. The XRD patterns of the *c*-BC_3 phase obtained under HPHT in the current study can be indexed with a cubic unit cell. It is probable that a different method of synthesis or another type of precursor is required to obtain the dense orthorhombic or tetragonal BC_3 phases predicted in Ref.[8].

The *dl*-BC_3 or *c*-BC_3 phases may behave as metals at ambient conditions[6] and are predicted to be superconductors at low temperatures[4, 5, 8]. If this is correct, it would be of interest to obtain *c*-BC_3 in relatively large amounts. One possible method is to use a large multi-anvil apparatus with a 6-8-2 cell, where recently a pressure close to 90 GPa was achieved[58]. Moreover, theoretical simulations conducted[1, 59] indicate that the energies of some BC_3 graphitic structures may be higher than that of the equivalent diamond-like phase. A low critical pressure of 4 GPa for a synthesis of the tetragonal BC_3 phase (originating from the cubic diamond structure) from the g-BC_3 is expected by Liu et al.[7]. Therefore, theoretical simulations allow us to suggest that low-pressure synthesis of the cubic BC_3 phase is possible. As suggested by Moussa, the kinetics of heating plays important role in *c*-BC_3 synthesis[38]. A plausible explanation for phase separation in the BC_3 system at 20 GPa and 2300 K[15] requires the diffusion of boron away from carbon. The primary diffusion channel in graphite is within the interstitial region between the graphitic planes. In the current research, we used high pressure to reduce the diffusion of the boron atoms between the graphitic planes. However, the diffusion of boron atoms can also be reduced by using other techniques. A short pulse laser, such as a nanosecond or picosecond laser, is used for synthesis of nanodiamonds[45, 60, 61]. It was found that the atomic-level structure of sp^3-bonded carbon nanoscale domains were formed dynamically from graphite by femtosecond-laser excitation[62]. This technique can be applied for synthesis of the *c*-BC_3 phase as well.

V. Conclusions

A diamond-like cubic phase, *c*-BC_3, was synthesized by direct transformation from a graphitic phase at a pressure of 39 GPa and temperature of 2200 K in a laser-heated diamond-anvil cell. Identification of the cubic phase and its stoichiometry were obtained from synchrotron

XRD, Raman spectroscopy, and TEM-EELS measurements. The zero-pressure lattice parameter of the *c*-BC_3 calculated from diffraction peaks was found to be a = 3.589 ± 0.007 Å. Using EELS measurements, the composition of the synthesized phase was determined to have a value of C/B ratio of approximately 3 (2.8 ± 0.7).

5. Acknowledgements

This work was supported by U.S. DOE grant NO. DE-FG02-07ER46408. The use of the HPCAT facility was supported by DOE-BES, DOE-NNSA (CDAC), NSF, DOD-TACOM, and the W.M. Keck Foundation. A portion of this work was performed at GeoSoilEnviroCARS (Sector 13), Advanced Photon Source (APS), Argonne National Laboratory. GeoSoilEnviroCARS is supported by the National Science Foundation-Earth Sciences (EAR-0622171) and Department of Energy-Geosciences (DE-FG02-94ER14466). Use of the APS was supported by the U.S. Department of Energy, Office of Science, Office of Basic Energy Sciences, under Contract No. DE-AC02-06CH11357. A portion of this work was performed under the auspices of the U.S. Department of Energy by Lawrence Livermore National Laboratory under Contract No. DE-AC52-09NA27344.

References

[1] J. E. Lowther, J. Phys. Condes. Matter. **17**, 3221 (2005).

[2] S. M. Nkambule and J. E. Lowther, Solid State Commun. **150**, 133 (2010).

[3] L. F. Xu, Z. S. Zhao, L. M. Wang, B. Xu, J. L. He, Z. Y. Liu, and Y. J. Tian, J. Phys. Chem. C **114**, 22688 (2010).

[4] J. E. Moussa and M. L. Cohen, Phys. Rev. B **74**, 094520 (2006).

[5] J. E. Moussa and M. L. Cohen, Phys. Rev. B **77**, 064518 (2008).

[6] J. Yang, H. Sun, J. L. He, Y. Tian, and C. F. J. Chen, J. Phys.: Condens. Matter **19**, 346223 (2007).

[7] Z. Y. Liu, J. L. He, J. Yang, X. J. Guo, H. Sun, H. T. Wang, E. Wu, and Y. J. Tian, Phys. Rev. B **73**, 172101 (2006).

[8] H. Y. Liu, Q. A. Li, L. Zhu, and Y. M. Ma, Phys. Lett. A **375**, 771 (2011).

[9] Y. C. Liang, W. Q. Zhang, J. Z. Zhao, and L. F. Chen, Phys. Rev. B **80**, 113401 (2009).

[10] M. Calandra and F. Mauri, Phys. Rev. Lett. **101**, 016401 (2008).

[11] Q. A. Li, H. Wang, Y. J. Tian, Y. Xia, T. A. Cui, J. L. He, Y. M. Ma, and G. T. Zou, J. Appl. Phys. **108**, 023507 (2010).

[12] H. Y. Liu, Q. A. Li, L. Zhu, and Y. M. Ma, Solid State Commun. **151**, 716 (2011).

[13] B. W. Dong, F. B. Tian, D. F. Duan, X. L. Jin, T. A. Cui, and G. T. Zou, Diam. Relat. Mat. **20**, 454 (2011).

[14] L. F. Xu, Z. S. Zhao, Q. Q. Wang, L. M. Wang, B. Xu, J. L. He, and Y. J. Tian, J. Appl. Phys. **110**, 013501 (2011).

[15] V. L. Solozhenko, N. A. Dubrovinskaia, and L. S. Dubrovinsky, Appl. Phys. Lett. **85**, 1508 (2004).

[16] P. V. Zinin, L. C. Ming , I. Kudryashov, N. Konishi, M. H. Manghnani, and S. K. Sharma, J. Appl. Phys. **100**, 013516 (2006).

[17] P. V. Zinin, L. C. Ming, I. Kudryashov, N. Konishi, and S. K. Sharma, J. Raman Spectrosc. **38**, 1362 (2007).

[18] P. V. Zinin, I. Kudryashov, N. Konishi, L. C. Ming, V. L. Solozhenko, and S. K. Sharma, Spectrochim. Acta, Part A. **61**, 2386 (2005).

[19] V. L. Solozhenko, O. O. Kurakevych, D. Andrault, Y. Le Godec, and M. Mezouar, Phys. Rev. Lett. **102**, 015506 (2009).

[20] L. C. Ming, P. V. Zinin, X. R. Liu, Y. Nakamoto, and R. Jia, J. Phys.: Conf. Ser. **215**, 012135 (2010).

[21] P. V. Zinin, L. C. Ming, S. K. Sharma, S. M. Hong, Y. Xie, T. Irifune, and T. Shinmei, J. Phys.: Conf. Ser. **121** 062002 (2008).

[22] Y. Zhao, D. W. He, L. L. Daemen, T. D. Shen, R. B. Schwarz, Y. Zhu, D. L. Bish, J. Huang, J. Zhang, G. Shen, J. Qian, and T. W. Zerda, J. Mater. Res. **17**, 3139 (2002).

[23] F. Langenhorst and V. L. Solozhenko, Phys. Chem. Chem. Phys. **4**, 5183 (2002).

[24] T. Shirasaki, A. Derre, M. Menetrier, A. Tressaud, and S. Flandrois, Carbon **38**, 1461 (2000).

[25] V. B. Prakapenka, A. Kubo, A. Kuznetsov, A. Laskin, O. Shkurikhin, P. Dera, M. L. Rivers, and S. R. Sutton, High Pressure Res. **28**, 225 (2008).

[26] G. Y. Shen, M. L. Rivers, Y. B. Wang, and S. R. Sutton, Rev. Sci. Instrum. **72**, 1273 (2001).
[27] P. V. Zinin, L. C. Ming, S. K. Sharma, Y. Liu, and S. M. Hong, Diam. Relat. Mat. **18**, 1123 (2009).
[28] R. E. Franklin, Acta Crystallogr. **4**, 253 (1951).
[29] R. E. Franklin, Proc. R. Soc. London, Ser. A **209**, 196 (1951).
[30] B. E. Warren, Phys. Rev. **59**, 693 (1941).
[31] M. Chasmawala and T. C. Chung, Carbon **35**, 641 (1997).
[32] T. Sasaki, M. Akaishi, S. Yamaoka, Y. Fujiki, and T. Oikawa, Chem. Mat. **5**, 695 (1993).
[33] B. Ottaviani, A. Derre, E. Grivei, O. A. M. Mahmoud, M. F. Guimon, S. Flandrois, and P. Delhaes, J. Mater. Chem. **8**, 197 (1998).
[34] O. O. Kurakevych, T. Chauveau, and V. L. Solozhenko, J. Superhard Mater. **32**, 231 (2010).
[35] J. E. Lowther, P. V. Zinin, and L. C. Ming, Phys. Rev. B **79**, 033401 (2009).
[36] F. Tuinstra and J. L. Koenig, J. Chem. Phys. **53**, 1126 (1970).
[37] R. J. Nemanich and S. A. Solin, Phys. Rev. B **20**, 392 (1979).
[38] J. E. Moussa, Private communication, 8 (2009).
[39] J. L. Zhou, T. Cui, Y. M. Ma, Z. M. Liu, B. B. Liu, and G. T. Zou, Chinese Phys. Lett. **23**, 2538 (2006).
[40] I. Suarez-Martinez, A. A. El-Barbary, G. Savini, and M. I. Heggie, Phys. Rev. Lett. **98**, 015501 (2007).
[41] E. Bustarret, E. Gheeraert, and K. Watanabe, Phys. Status Solidi A **199**, 9 (2003).
[42] S. Prawer and R. J. Nemanich, Proc. R. Soc. London, Ser. A **362**, 2537 (2004).
[43] L. Niu, J. Q. Zhu, X. Han, M. L. Tan, W. Gao, and S. Y. Du, Phys. Lett. A **373**, 2494 (2009).
[44] J. Ruvalds and A. Zawadowski, Phys. Rev. B **2**, 1172 (1970).
[45] M. Nesladek, D. Tromson, C. Mer, P. Bergonzo, P. Hubik, and J. J. Mares, Appl. Phys. Lett. **88**, 232111 (2006).
[46] S. Prawer, K. W. Nugent, D. N. Jamieson, J. O. Orwa, L. A. Bursill, and J. L. Peng, Chem. Phys. Lett. **332**, 93 (2000).
[47] E. Knittle, R. B. Kaner, R. Jeanloz, and M. L. Cohen, Phys. Rev. B **51**, 12149 (1995).
[48] V. L. Solozhenko, D. Andrault, G. Fiquet, M. Mezouar, and D. C. Rubie, Appl. Phys. Lett. **78**, 1385 (2001).
[49] H. W. Hubble, I. Kudryashov, V. L. Solozhenko, P. V. Zinin, S. K. Sharma, and L. C. Ming, J. Raman Spectrosc. **35**, 822 (2004).
[50] A. Sikora, O. Bourgeois, J. C. Sanchez-Lopez, J. N. Rouzaud, T. C. Rojas, A. S. Loir, J. L. Garden, F. Garrelie, and C. Donnet, Thin Solid Films **518**, 1470 (2009).
[51] V. Serin, R. Brydson, A. Scott, Y. Kihn, O. Abidate, B. Maquin, and A. Derre, Carbon **38**, 547 (2000).
[52] K. M. Krishnan, Appl. Phys. Lett. **58**, 1857 (1991).
[53] S. Suzuki, M. Tomita, and T. Hayashi, Jpn. J. Appl. Phys. Part 2 - Lett. **34**, L191 (1995).
[54] L. A. J. Garvie, H. Hubert, W. T. Petuskey, P. F. McMillan, and P. R. Buseck, J. Solid State Chem. **133**, 365 (1997).
[55] K. Hofmann, R. Gruehn, and B. Albert, Z. Anorg. Allg. Chem. **628**, 2691 (2002).
[56] I. Caretti, R. Gago, J. M. Albella, and I. Jimenez, Phys. Rev. B **77**, 6 (2008).

[57] V. L. Solozhenko, O. O. Kurakevych, D. Andrault, Y. Le Godec, and M. Mezouar, Phys. Rev. Lett. **102**, 179901 (2009).
[58] T. Kunimoto, T. Irifune, and H. Sumiya, High Press. Res. **28**, 237 (2008).
[59] J. E. Lowther, Materials **4**, 1104 (2011).
[60] D. H. Lowndes, D. B. Geohegan, A. A. Puretzky, D. P. Norton, and C. M. Rouleau, Science **273**, 898 (1996).
[61] C. X. Wang, P. Liu, H. Cui, and G. W. Yang, Appl. Phys. Lett. **87**, 201913 (2005).
[62] J. Kanasaki, E. Inami, K. Tanimura, H. Ohnishi, and K. Nasu, Phys. Rev. Lett. **102**, 087402 (2009).

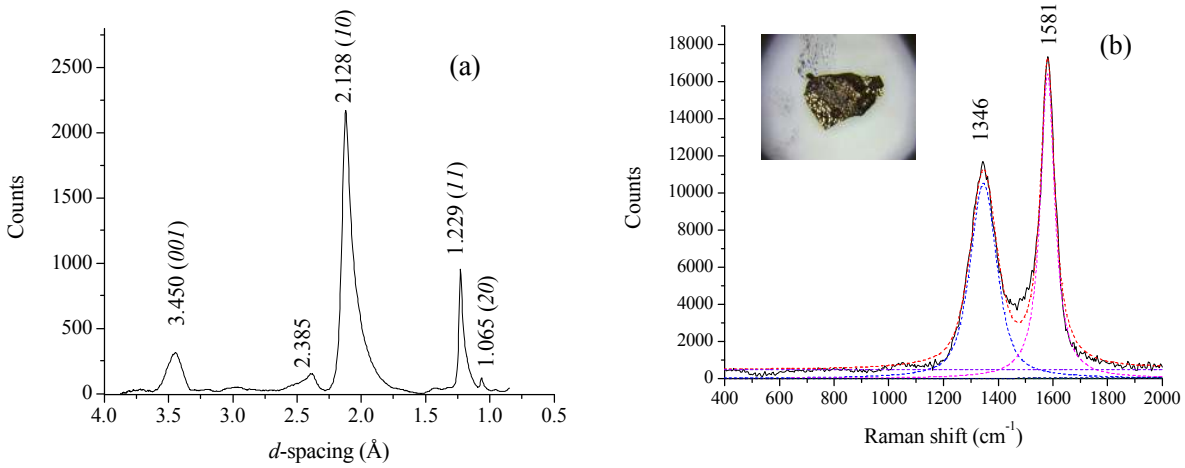

Figure 1. XRD and Raman scattering characterization of the starting material, g-BC3: (a) XRD pattern (λ = 0.3447 Å); (b) Raman spectrum (λ=532 nm). Power was 0.2 mW and collection time was 20 s. The solid line is the measured Raman spectrum; varicolored dashed Gaussian shaped peaks are the result of the Grams software fitting. Insert is the optical image of the graphitic BC3 phase taken with an objective x50. The size of the image is 250 x 250 µm.

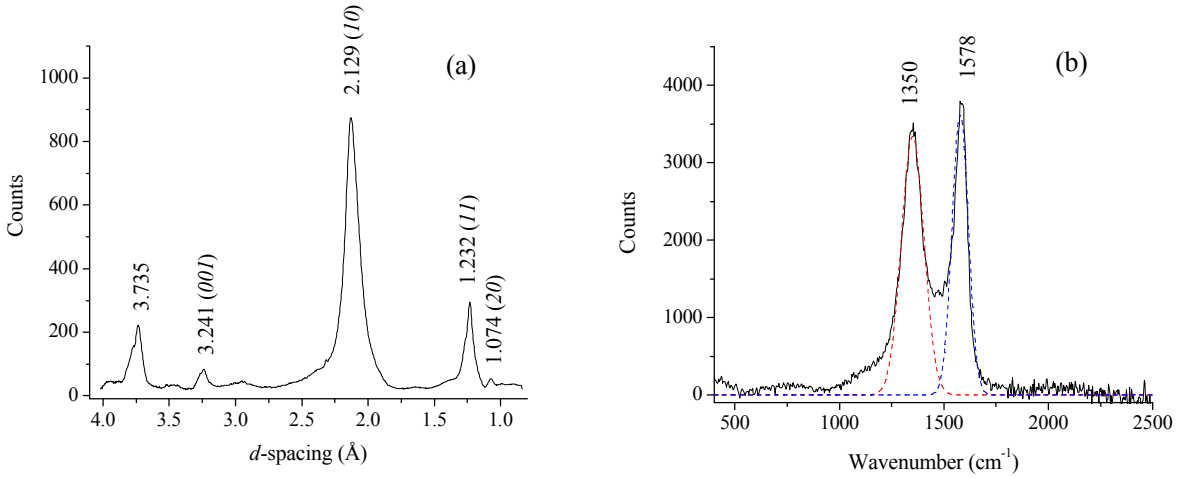

Figure 2. XRD and Raman scattering characterization of specimen *A*, BC_3 phase recovered from 24 GPa after heating at 2020 K. (a) The ambient XRD pattern (λ = 0.3681 Å) and (b) Raman spectrum (532 nm). Power was 2 mW and the integration time was 1.5 min. Notations for the Raman lines are the same as in Fig. 1a.

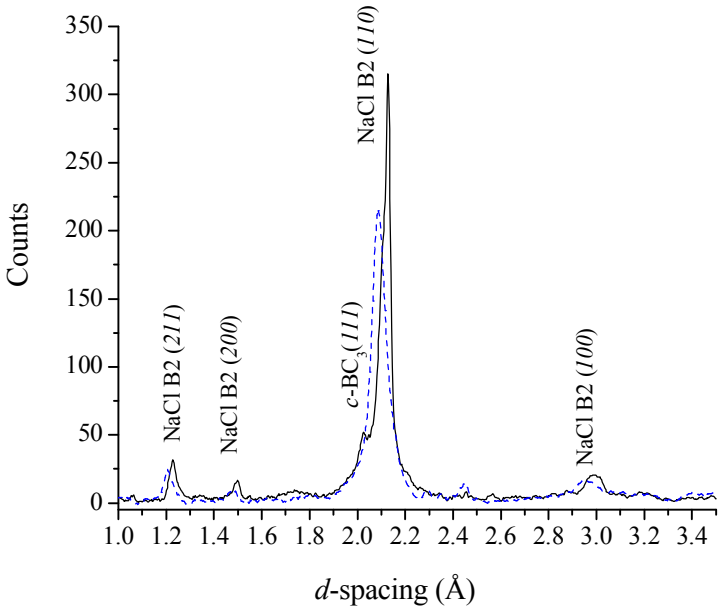

Figure 3. XRD patterns (λ = 0.3681 Å) of specimen *B* collected before (44 GPa, dashed line) and after (37 GPa, solid line) laser heating at temperature 1980 K.

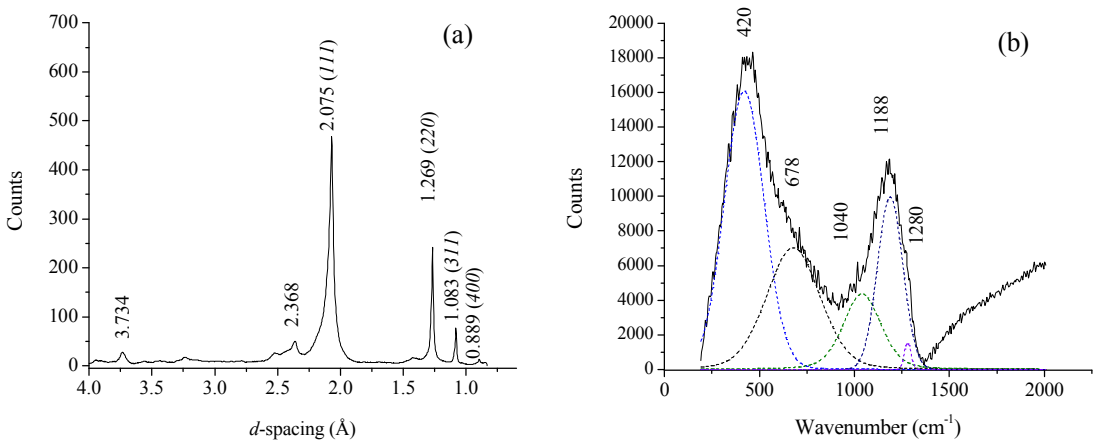

Figure 4. XRD and Raman scattering characterization of specimen *B*, *c*-BC_3 phase recovered from 44 GPa after heating at 1980 K. (a) The ambient XRD pattern (λ = 0.3681 Å) and (b) Raman spectrum (514 nm) of *c*-BC_3 phase. Integration time was 2.5 min and laser power was 2 mW. Notations for the Raman lines are the same as in Fig. 1a.

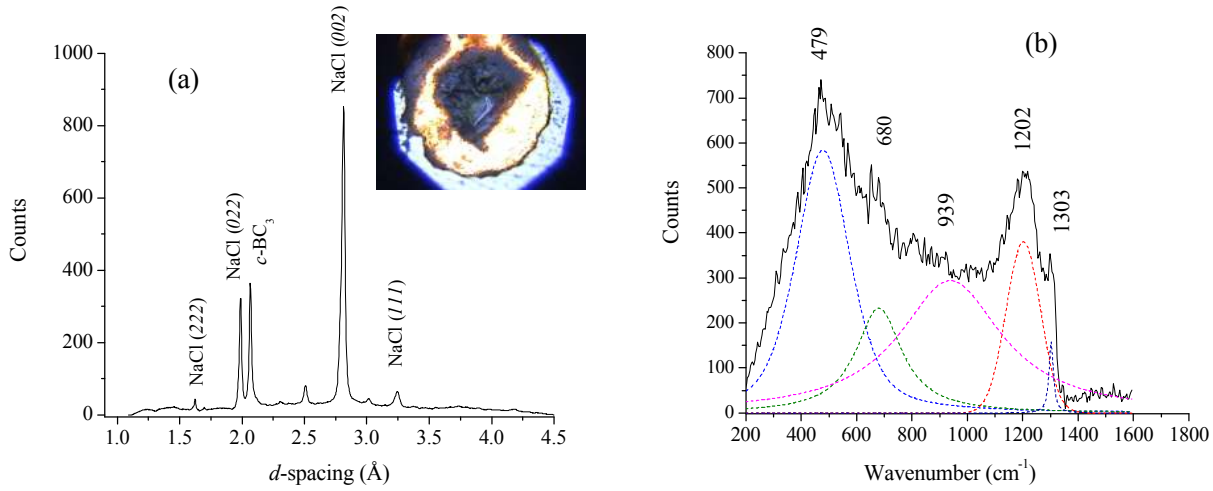

Figure 5. XRD and Raman scattering characterization of specimen *C, c*-BC_3 phase recovered from 39 GPa after heating at 2200 K. (a) The ambient XRD pattern (λ = 0.3344 Å). Insert is an optical image of the specimen in a gasket filled with epoxy resin. The optical image was taken in transmission light configuration with an objective x50. The size of the image is 100 x 100 μm. (b) Raman spectrum (514 nm). Integration time 15 min and laser power 3 mW. Notations for the Raman lines are the same as in Fig. 1a.

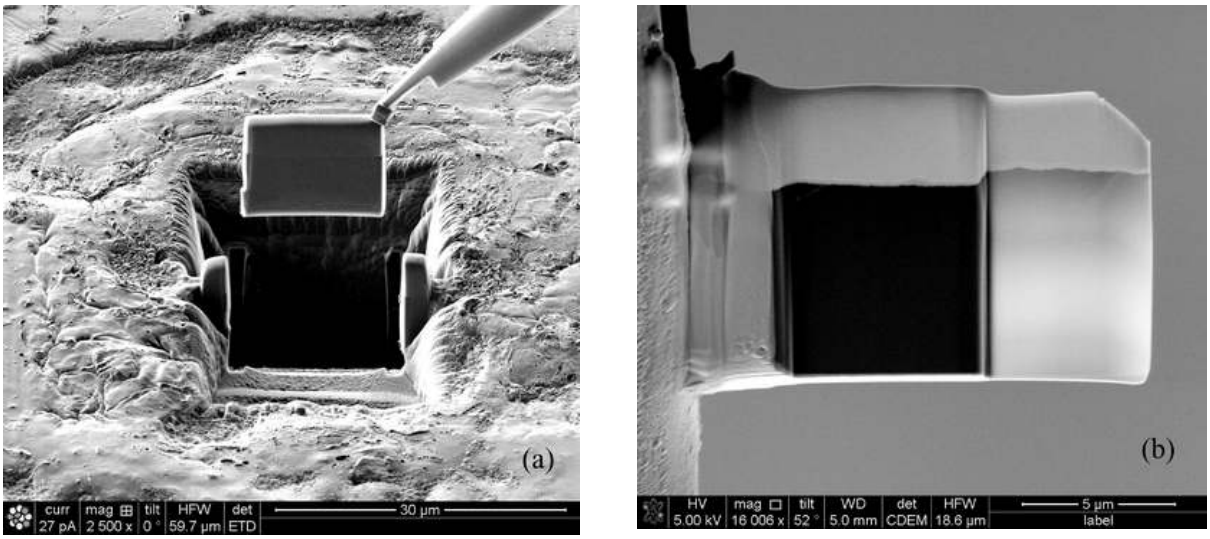

Figure 6. Focused ion beam (FIB) preparation of a TEM specimen. (a) Secondary ion image of the removal of a small section of the *c*-BC_3 phase on an *in situ* micromanipulator in the FIB. (b) Secondary electron image of the section after attachment to a TEM half-grid and thinning of a portion to ~50 nm (electron transparent for TEM analyses).

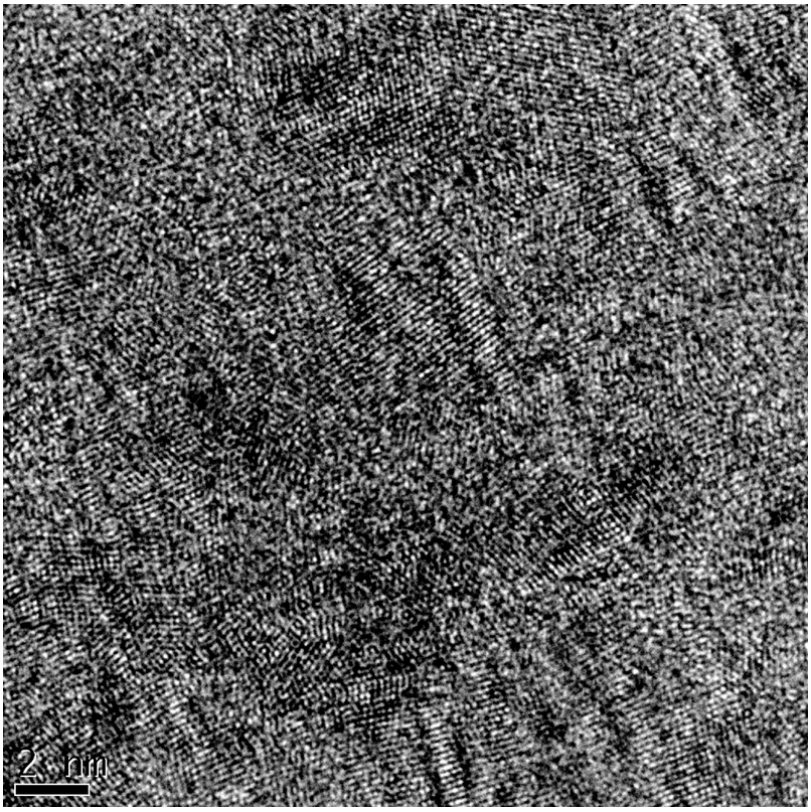

Figure 7. High resolution TEM image of the *c*-BC_3 phase.

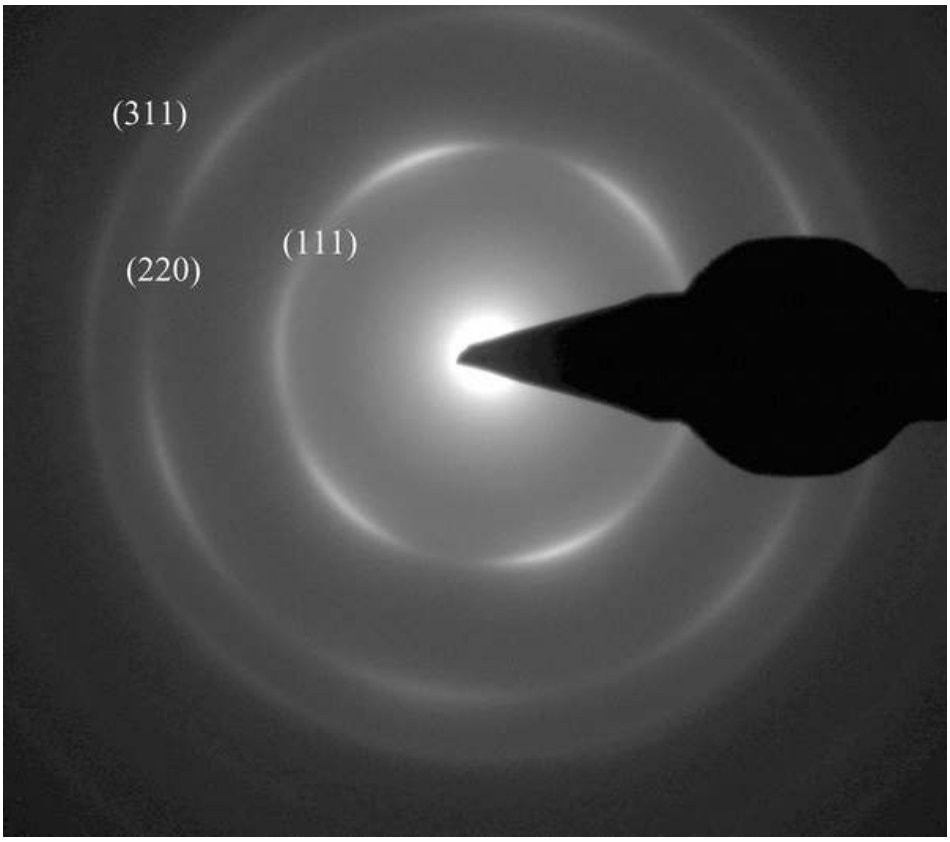

Figure 8. Selected area electron diffraction pattern of an area of the nanocrystalline *c*-BC_3 phase. The three readily distinguishable diffraction rings correspond to the (*111*), (*220*), and (*311*) reflections.

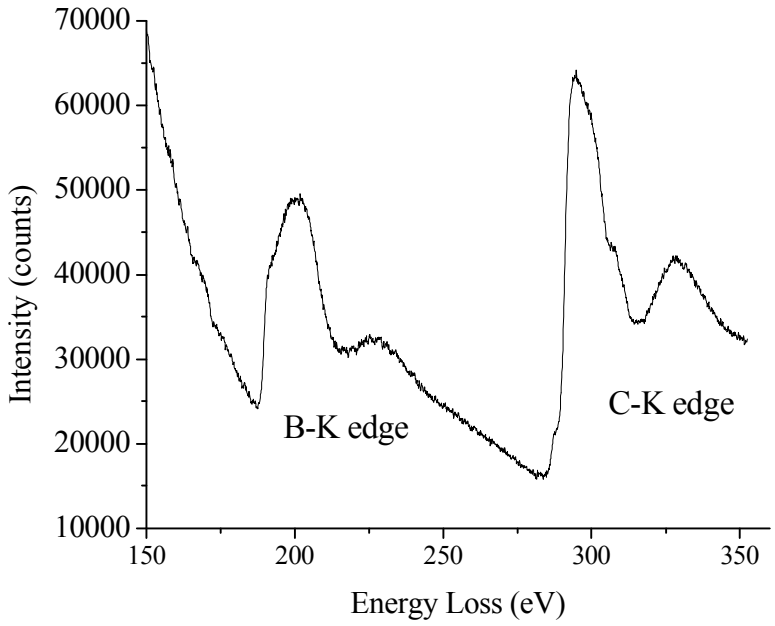

Figure 9. Electron energy loss spectrum of the final *c*-BC_3 phase. The spectrum was collected at 0.1 eV/channel with 0.9 eV energy resolution.